

Evolution of the buoyant bubbles in M87

E.Churazov^{1,2}, M.Brüggen^{1,3}, C.R.Kaiser¹, H.Böhringer⁴, W.Forman⁵

ABSTRACT

The morphology of the X-ray and radio emitting features in the central ~ 50 kpc region around the galaxy M87 strongly suggests that buoyant bubbles of cosmic rays (inflated by an earlier nuclear active phase of the galaxy) are slowly rising through the cooling gas. In the absence of strong surface tension, an intrinsic property of initially spherical bubbles is their transformation into tori as they rise through an external medium. Such structures can be identified in the radio images of the halo of M87. During their rise the bubbles uplift relatively cool X-ray emitting ambient gas from the central regions of the cooling flow to larger distances. This gas is colder than the ambient gas and has a higher volume emissivity. As a result, rising “radio” bubbles may be trailed by elongated X-ray features as indeed is observed in M87. We performed simple hydrodynamical simulations in order to qualitatively illustrate the evolution of the buoyant bubbles in the M87 environment.

Subject headings: galaxies: active - galaxies: clusters: individual: Virgo - cooling flows - galaxies: individual: M87 - X-rays: galaxies

1. Introduction

The giant elliptical galaxy M87 continues to be the subject of numerous experimental and theoretical studies. It is located at, or near, the center of the very nearby (~ 18 Mpc, 1 arcminute corresponds to ~ 5 kpc) irregular Virgo cluster and is a center of a weak cooling flow with a mass deposition rate of some $10\text{--}40 M_{\odot}$ per year (e.g. Peres et al. 1998). The radio source Virgo A (3C274) associated with the galaxy M87 is well known, in particular because of the spectacular jet which is observed both in radio and optical bands (see e.g. Biretta 1999 for a review). In addition to the jet, which is contained within the central 2 kpc or $30''$ region, there is a lower surface brightness

radio halo extending up to a distance of $\sim 40\text{--}50$ kpc from the nucleus (e.g. Kassim et al. 1993, Böhringer et al. 1995, Owen, Eilek and Kassim 1999, 2000).

The X-ray emission is strongly peaked at the position of the nucleus of M87 and is largely symmetric around it. However, it was found in the Einstein HRI observations (Feigelson et al. 1987) and then in the ROSAT data (Böhringer et al. 1995) that there are departures from a symmetric model and these departures resemble the morphology of the some prominent features in the outer radio lobes. These findings initiated numerous discussions on the interaction of the radio and X-ray emitting plasmas (e.g. Feigelson et al. 1987, Böhringer et al. 1995, Böhringer et al. 1999, Owen, Eilek and Kassim 1999, 2000, Harris et al., 1999). In a number of other cooling flow clusters with strong radio halos surrounding the dominant galaxy (e.g. Perseus – Böhringer et al. 1993, McNamara et al. 1996, Churazov et al. 2000, Fabian et al. 2000, A4059 – Huang and Sarazin 1998, Hydra A – McNamara et al. 2000) there is a clear anticorrelation of the radio and X-ray emitting plasmas. This makes the case of M87 especially interesting.

¹MPI für Astrophysik, Karl-Schwarzschild-Strasse 1, 85740 Garching, Germany

²Space Research Institute (IKI), Profsouznaya 84/32, Moscow 117810, Russia

³Churchill College, Storey’s Way, Cambridge CB3 0DS, United Kingdom

⁴MPI für Extraterrestrische Physik, P.O.Box 1603, 85740 Garching, Germany

⁵Harvard-Smithsonian Center for Astrophysics, 60 Garden St., Cambridge, MA 02138

We discuss below one particular model which is able to reproduce qualitatively both the radio and X-ray morphologies observed in the central region surrounding the M87 galaxy.

1.1. Radio and X-ray morphology

There is a long history of M87 radio halo observations, starting with Mills (1952) shortly after the initial discovery of the radio source Virgo A (Bolton, Stanley and Slee 1949). Because of the very bright compact source the dynamic range of the images was always a problem. Recently, Owen et al. (2000) presented a new high resolution, high dynamic range map of the halo of M87 at 327 MHz (see Figure 1). For the sake of further discussion this map has been rotated by 90 degrees to have East up and North to the right. In this map several distinct structures are discernible. The high brightness centre represents the well-studied inner lobe structure (oriented approximately north-south) with the famous jet pointing west northwest (approximately bottom-right for the orientation of images adopted in Fig.1). Surrounding this, the highly structured outer halo is much fainter. It consists of the ear-shaped (torus-like) eastern bubble, the much less well-defined western bubble, both of which are connected to the central emission by a ‘trunk’, and the two very faint almost circular emission regions northeast and southwest of the centre.

Owen et al. (2000) find a peak surface brightness in the region of the eastern bubble of about 53 mJy/beam while the circular regions range from 14 mJy/beam to about 25 mJy/beam. Rottmann et al. (1996) show that all of the described structures are also present at 10.6 GHz. They also show that the outer halos have a radio spectral index in the range from -2.8 to -2.5 between 4.8 GHz and 10.6 GHz. The spectral index is flatter by a factor of about 1.5 between 330 MHz and 1.5 GHz. This suggests that radiative energy losses of the synchrotron emitting particles lead to a significant steepening of the radio spectrum at about 3 GHz. Unfortunately, the maps used by Rottmann et al. (1996) have low resolution as they are obtained with single dish observations and so the spectral index distribution of the halo and its connection to the detailed structures, e.g., bubbles and attached “trunks”, is not known.

Detailed measurements of the Faraday rotation of the polarised emission of the inner lobes are presented in Owen et al. (1990). They find rotation measures (RM) of about 2000 rad m^{-2} towards the eastern inner lobe and 750 rad m^{-2} towards the western inner lobe. A large region of the eastern lobe shows peak RM in excess of 6000 rad m^{-2} while towards the inner jet in the western lobe the RM is only about 200 rad m^{-2} . Owen et al. (1990) argue that the average RM arises from a Faraday screen about 1 kpc thick which envelopes the inner lobe structure. This implies magnetic field strengths in this layer of about $40 \mu\text{G}$.

In Fig.1 (lower left) we show the X-ray surface brightness distribution of the same region (and similar orientation). The data are the combined 200 ksec ROSAT/HRI image, adaptively smoothed to suppress high frequency noise. As pointed out by a number of authors (Feigelson et al. 1987, Böhringer et al. 1995, Owen, Eilek and Kassim 1999, Harris et al. 1999) there is evidence for a correlation between X-ray and radio emitting features. The simplest explanation of this correlation is that the excess X-ray emission is due to inverse Compton scattering of the cosmic microwave background photons by the same relativistic electrons which produce the synchrotron radio emission (Feigelson et al. 1987). But ROSAT/PSPC observations have shown that the excess emission has a thermal spectrum (Böhringer et al. 1995) and the X-ray emitting gas in these region has a lower temperature than that in the ambient regions.

Thus we summarize three observational facts which we are trying to explain below:

- There are prominent “torus-like” features in the radio image.
- There is a correlation (but not one to one) of the X-ray and radio bright regions.
- Excess X-ray emission, associated with the radio bubbles and attached “trunks”, arises from thermal gas whose temperature is less than that of the ambient X-ray emitting gas.

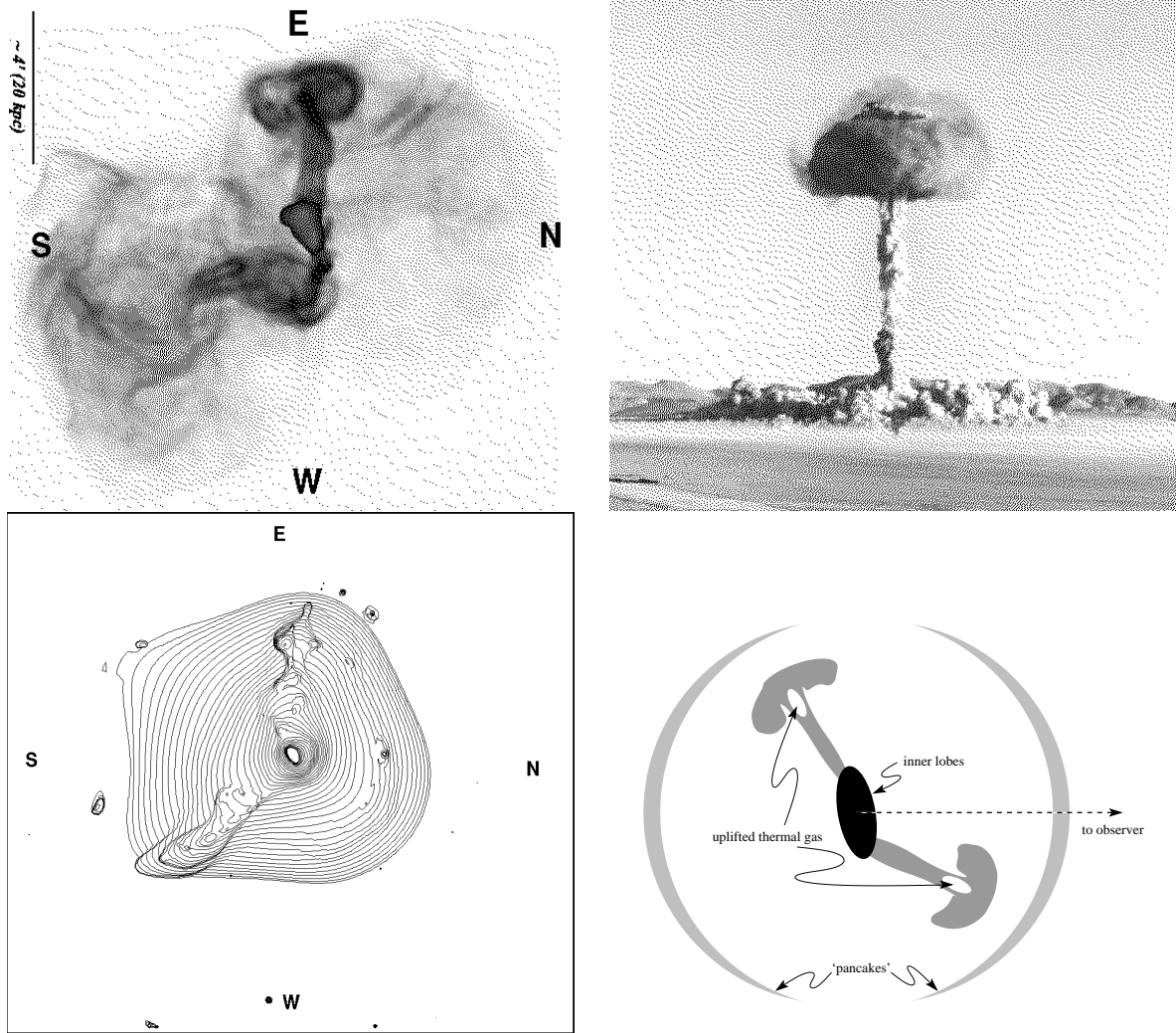


Fig. 1.— **Top-Left:** $14'.6 \times 16'.0$ map of the radio halo of M87 at 327 MHz rotated 90° clockwise (North is to the right, East is up). The map was kindly provided by F.Owen (see Owen, Eilek and Kasim 2000 for original data). **Top-Right:** Nuclear explosion in the Earth's atmosphere. Adopted from <http://www.enviroweb.org>. **Bottom-Left:** Adaptively smoothed ROSAT HRI X-ray image. The size and orientation of the image are the same as for the radio image. **Bottom-Right:** Possible geometry of the source inspired by the analogy with a powerful atmospheric explosion. The black region in the center denotes the inner radio lobes, gray ‘mushrooms’ correspond to the buoyant bubbles already transformed into tori, and the gray lens-shaped structures are the ‘pancakes’ formed by the older bubbles. To explain the observed morphology, the source must be oriented close to the line of sight (dashed line). The pancakes are shown edge-on as shaded regions.

1.2. Analogy with nuclear explosions

Concentrating on the “torus-like” radio features one can note its striking similarity with some evolutionary stages of hot buoyant bubbles formed by a powerful (e.g. nuclear) explosion in the Earth’s atmosphere (see Fig.1). Transformation of the initially spherical bubble into a torus is a common and well known property of buoyant bubbles lacking strong surface tension (e.g. Walters and Davison 1963, Onufriev 1967, Zhidov et al. 1977). Morphologically similar structures resembling “mushrooms” appear in Rayleigh-Taylor unstable configurations: as the fluid rises through the ambient medium, Kelvin-Helmholtz instabilities create the torus-like head of the “mushroom”. The idea that buoyancy plays an important role in the evolution of the radio lobes in galaxies has been first proposed by Gull and Northover (1973) and has been used to estimate the life time of the radio lobes in M87 by Böhringer et al. (1995). The similarity of the M87 “torus-like” features to the Rayleigh-Taylor mushrooms was pointed out by Churazov et al. (2000) and to the subsonic vortex ring by Owen, Eilek and Kassim (2000).

Further pursuing the analogy with powerful explosions, we note that during the transformation of a bubble into a torus some ambient gas is captured and uplifted by the by the rising bubble/torus. In the cooling flow surrounding M87, the entropy of the X-ray emitting gas rises quickly with distance from the centre, and therefore the emissivity of the gas increases very steeply if it remains in pressure balance with the ambient gas (Böhringer et al. 1995, Nulsen 1997). This may qualitatively explain the correlation of the radio and X-ray emitting plasmas and naturally accounts for the thermal nature of the excess thermal emission.

In the case of an atmospheric explosion the final stage of the hot bubble occurs when the bubble reaches a height at which the density of the ambient gas is equal to the density of the bubble. Then (neglecting oscillations near the equilibrium position) the bubble expands laterally (forming a “pancake”) in order to occupy that thin layer in the atmosphere having the same density. The bubbles/tori in M87 may share the same fate. In a spherically symmetric potential, the bubble will

try to fill a segment (equipotential surface) of the sphere. The largest distinct features in the radio map (see Fig.1) could be just those late-stage bubbles.

The sketch of the possible overall source structure based on the analogy with a powerful atmospheric explosion is shown in Fig.1. Here the black region in the center denotes the inner radio lobes, the gray mushrooms correspond to the buoyant bubbles already transformed into tori and the gray lens-shaped structures are the “pancakes” formed by the older bubbles.

Buoyant bubbles and their role in the complex X-ray and radio morphology of M87 have been discussed previously e.g. in Böhringer et al. 1995, Nulsen 1997, Böhringer 1999, Owen, Eilek and Kassim 2000. Below we follow the line of arguments suggested in Churazov et al. (2000) and present hydrodynamical calculations of the radio lobe evolution in order to illustrate the qualitative picture described above.

2. Method

2.1. Hydrodynamical simulations

The simulations were obtained using the ZEUS-3D code which was developed especially for problems in astrophysical hydrodynamics (Clarke & Norman 1994). The code uses finite differencing on an Eulerian grid and is fully explicit in time. It is based on an operator-split scheme with piecewise linear functions for the fundamental variables. The fluid is advected through a mesh using the upwind, monotonic interpolation scheme of van Leer. For a detailed description of the algorithms and their numerical implementation see Stone & Norman (1992a, b). In order to study the spectral ageing of the relativistic gas, the ZEUS code was modified to follow the motion of ‘tracer’ particles which are advected with the fluid.

In our simulations we employed an ideal gas equation of state and we ignored the effects of magnetic fields and rotation. The cooling time is sufficiently long compared to the time scales considered here since, for an electron density of 0.02 cm^{-3} and temperature of the order of 2 keV (see Fig. 2) the cooling time is $\sim 5 \times 10^8$ years. This is some orders of magnitude longer than the typical duration of the run of $\sim 5 \times 10^7$ years.

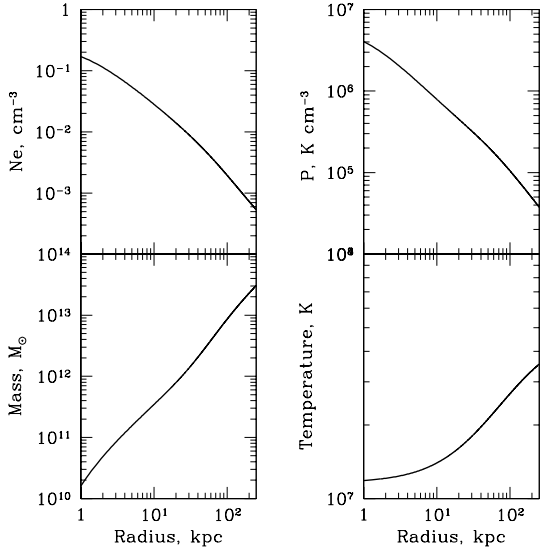


Fig. 2.— Initial distribution of electron density, temperature, pressure and gravitating mass (adopted from Nulsen and Böhringer 1995) assumed in the simulations.

We therefore completely neglected cooling. The simulations were computed on a spherical grid in two dimensions and were performed on an IBM RS/6000 cluster. The computational domain spans 51 kpc in radius and $\pi/2$ rad in angle and was covered by 200×200 grid points (in the r - and θ -direction).

A model for the mass and initial temperature was adopted from Nulsen & Böhringer (1995) which is shown in Fig.2. The gas density distribution was then found by assuming hydrostatic equilibrium to maintain an initially static model. A spherical bubble was set up with a radius of $r_b = 5$ kpc at a distance of $d = 9$ kpc from the gravitational center. It was made buoyant by lowering its density with respect to the background density by a factor of 100 and simultaneously rising the temperature by the same factor. During the subsequent evolution the gas which is treated as a single fluid was assumed to obey a polytropic equation of state with $\gamma = 5/3$. The bubble was filled with 2000 tracer particles and was placed on the $\theta = 0$ axis along which it rose

in the gravitational potential. Subsequently, we rotated the two-dimensional output about this axis (azimuthally). To test the assumption of rotational symmetry, we performed some 3D simulations with reduced resolution and found that this assumption is fairly robust as far as the global motions and morphologies are concerned. As we discuss in detail below, buoyancy deforms the bubble and drives it through the ambient medium as shown in Fig.3. Shear instabilities cause the formation of tori which separate from the main bubble. This process, also called “vortex shedding”, has been observed and studied extensively (see Norman et al. 1982).

Finally, we should address some issues related to the accuracy of these kinds of finite-difference hydrodynamical simulations. First, one can note that the density in the bubble decreases. While the code can simulate large-scale mixing due to Rayleigh-Taylor and Kelvin-Helmholtz instabilities, it does not include real diffusion of particles. Any observed diffusion is therefore entirely numerical. The boundary between the bubble and the ambient medium also becomes less sharp as the simulation proceeds due to discretization errors in the advection scheme. For a test of the advection algorithm in the ZEUS code see Stone & Norman (1992). In simple advection tests it was found that during the advection of a sharp discontinuity over a grid of 200 zones the discontinuity is spread over 3-4 grid cells. Therefore, the small features in our simulation are likely to be affected by these advection errors whereas the larger features are not.

Second, numerical viscosity is also responsible for suppressing small-scale instabilities at the interface between the bubble and the cooler, surrounding, X-ray emitting gas. To assess the effects of numerical viscosity, we have repeated our simulations on grids with 100×100 grid points. From our experiments we can conclude that “global parameters” such as the position and size of the bubble as well as the presence of “toroidal” structure are relatively insensitive to the resolution. The detailed developments of the morphology on small scales do depend on the resolution and the initial conditions.

Finally, we stress that the simulations presented here are not intended to provide a detailed simulation of the radio/X-ray structure surrounding

M87. Rather they are intended as a guide, a toy model, to assist our interpretation of the complex emission (see discussion in Section 3.1).

2.2. Simulation of the radio emission

The observations of radio synchrotron emission from the buoyant bubbles in M87 implies the presence of a relativistic, magnetised plasma. However, the simulations presented in previous sections are based on a purely hydrodynamical scheme with a single, non-relativistic fluid. To estimate the radio flux expected from the simulation, we make the following assumptions:

- The relativistic plasma and the associated magnetic field, the ‘relativistic fluid’, are confined within small volumina intermixed with the non-relativistic, thermal plasma governing the dynamics. This implies that the relativistic fluid may mix with the thermal fluid on macroscopic scales but not on microscopic ones. This is very similar to the situation of air bubbles in water which are confined by surface tension (e.g. Zhidov et al. 1977).
- The relativistic fluid is in pressure equilibrium with the thermal fluid and expands or contracts adiabatically with an adiabatic index $\Gamma_r = 4/3$. However, the relativistic fluid is dynamically passive in the sense that its behaviour does not alter the total fluid flow. We will see in the following that this assumption is probably invalid. Note also, that we assume the magnetic field to be tangled on scales much smaller than the physical scale of the problem. This allows us to treat the magnetic field as part of the relativistic fluid.
- At the start of the simulation the relativistic fluid is confined to the rarefied buoyant bubble of gas. The total energy density of the fluid is the sum of the energy density of the magnetic field, u_B , and that of the relativistic particles, u_e . In practice we will assume an initially uniform magnetic field strength throughout the bubble and match the thermal pressure, p_{th} , acting on the relativistic fluid by adjusting the energy density of the relativistic particles, i.e. $3p_{th} = u_B + u_e$.

- There is no significant re-acceleration of relativistic particles in the bubble.

These assumptions fully determine the state of the relativistic fluid at any given point in the simulation at all times. Nevertheless, the synchrotron emission also depends on the energy distribution of the relativistic particles. Initially we assume that this is given by a power law which can be expressed in terms of the particle Lorentz factor, γ , $n_e(t_o)d\gamma = n_o\gamma^{-p}d\gamma$. The energy losses of the relativistic particles due to adiabatic expansion, synchrotron radiation and inverse Compton scattering of the CMB will modify this simple power law. The radiative energy losses produce a break in the radio synchrotron spectrum. Significant steepening of the spectrum will be observed for frequencies higher than the break frequency, ν_{break} . For a constant magnetic field this is given by (e.g. Leahy 1991)

$$\nu_{break} = 2.52 \cdot 10^6 \frac{B}{(B^2 + B_{CMB}^2)^2 t^2} \text{ GHz}, \quad (1)$$

where B is the strength of the magnetic field in μG and t is the time for which the plasma was exposed to this field in Myrs. B_{CMB} is the strength of the magnetic field in μG equivalent to the energy density of the CMB, u_{IC} . For the redshift of M87, $u_{IC} \sim 4.2 \cdot 10^{-13} \text{ erg cm}^{-3}$ and so $B_{CMB} \sim 3.2 \mu\text{G}$.

However, the energy loss processes depend on the local conditions, most notably the strength of the magnetic field, in the relativistic fluid at a given time. To improve on the estimate for the emitted spectrum provided by equation 1 we use the tracer particles, initially uniformly distributed throughout the rarefied bubble, to follow the evolution of the local pressure in the bubble. Because of our assumption of approximate pressure equilibrium, the knowledge of the thermal pressure completely determines the properties of the relativistic fluid, i.e. $u_B(t) = u_B(t_o)[p_{th}(t)/p_{th}(t_o)]$. Between numerical time steps we interpolate linearly so that at the i -th time step $dp_{th}/dt = [p_{th}(t_{i+1}) - p_{th}(t_i)]/\Delta t$, where Δt is the length of one time step. Using the pressure history of the tracer particles we can then construct the energy distribution of the relativistic particles iteratively from time step to time step by integrating the energy loss equation (e.g. Kaiser, Dennett-

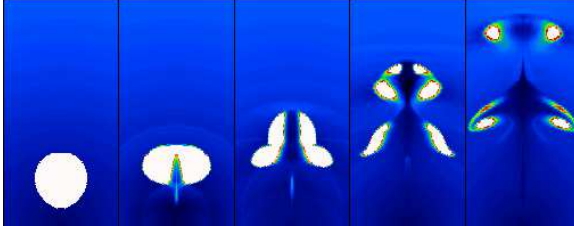


Fig. 3.— Temperature distribution in the gas at 5 time steps. From left to right: 0, 8.4, 21, 42 and 67 Myrs after the start of the simulation. Each box is 40 by 20 kpc. The center of the cluster is at the bottom of the box. Temperature is color coded in the 0.7 (black) to 5 keV (white) range. The temperature of the cluster thermal gas (blue) changes from ~ 1 keV at the center to ~ 1.7 keV at a distance of 40 kpc. All temperatures above 5 keV are white. Thus, the hot “radio-emitting plasma” which initially has a temperature of order of 100 keV is white. Numerical diffusion (due to very strong gradients in density and temperature) creates regions with intermediate values of temperature (yellow, red, green) along the boundaries of the bubble. Note that during later stages the coldest gas is not at the centre of the cooling flow, but is associated with the rising bubble. Since radiative cooling was not included in the simulations these cold regions are due to the uplifted (and adiabatically expanded) gas.

Thorpe & Alexander 1997). Finally, the energy distribution of the relativistic particles combined with the strength of the magnetic field yields the synchrotron emissivity (e.g. Longair 1991). To obtain the synchrotron surface brightness from the simulation we assume rotational symmetry about the polar-axis and integrate the emissivity along lines of sight through the resulting 3-dimensional model.

3. Results and discussion

3.1. Bubble configuration

Shown in Fig.3 are snapshots of the temperature distribution during the evolution of the bubble. One can identify two stages of the bubble evolution. The initially spherical bubble flattens and develops a “cone” at the rear, which is filled with entrained gas. The bubble then transforms

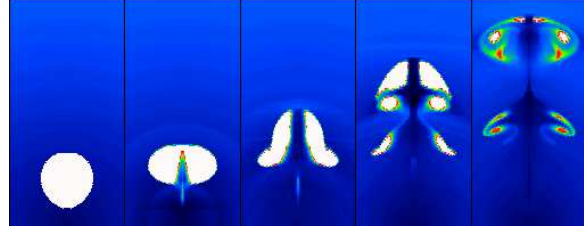


Fig. 4.— The same as in the previous figure but with an initial temperature contrast, between the ambient gas and the bubble, which is a factor of two larger. Note that detailed morphology of the rising bubble is rather sensitive to the initial conditions (and boundary conditions, symmetry assumed etc.) and can be very different from what is shown in these figures. The presence of the torus-like structure is, however, a generic feature of the rising bubble phenomenon.

into a torus which at later stages may fragment into smaller structures, but which continue to show a global toroidal structure. Note that ambient gas (in particular the gas captured during the bubble \rightarrow torus transformation) occupies the central part of the rising structure. Note also that in the last stages (shown in Fig.3) the coldest temperatures are found not at the center of the cluster but within the rising structure. We stress again that no radiative cooling was included in the simulations and these low temperatures regions are associated with gas which has been uplifted from the central regions and has expanded adiabatically to match the ambient gas pressure at the current location of the bubble.

Of course the particular shape of the torus/mushroom structure (e.g. two tori at different distances from the center in Fig.3) is the result of our choice of initial and boundary conditions and assumed axial symmetry. In general one would expect a large variety of structure to be formed, especially in 3D. But the torus-like geometry is a generic feature of rising bubbles in the absence of strong surface tension.

3.2. The velocity of the rising bubble

The simplest velocity estimate of the rising bubble can be obtained by equating the ram pressure and buoyancy forces acting upon a bubble (e.g.

Gull and Northover 1973). The buoyancy force is obviously:

$$F_b = Vg(\rho_a - \rho_b), \quad (2)$$

where V is the bubble volume, g is the gravitational acceleration (we assume the ambient gas is in the hydrostatic equilibrium), ρ_a and ρ_b are the mass densities of the ambient and the bubble gas densities respectively. The ram pressure (drag) is:

$$F_d \sim C \frac{1}{2} S v^2 \rho_a, \quad (3)$$

where S is the cross section of the bubble. A numerical coefficient C (drag coefficient) depends on the geometry of the bubble and the Reynolds number. For a solid sphere moving through an incompressible fluid this coefficient is of the order 0.4–0.5 for Reynolds numbers in the range $\sim 10^3$ – 10^5 (e.g. Landau and Lifshitz 1963). Thus the terminal velocity of the bubble is

$$v \sim \sqrt{g \frac{V}{S} \frac{2}{C} \frac{\rho_a - \rho_b}{\rho_a}} \sim \sqrt{g \frac{V}{S} \frac{2}{C}}. \quad (4)$$

Here the factor of $(\rho_a - \rho_b)/\rho_a$ can be dropped if the bubble density is low compared to the ambient gas density. The expression for the terminal velocity can be further rewritten using the Keplerian velocity at a given distance from the cluster center: $v \sim \sqrt{(r/R)(8/3C)} v_K$, where r is the bubble radius, R is the distance from the center and $v_K = \sqrt{gR}$ is the Keplerian velocity. Of course the above formula can be used only for order of magnitude estimates of the bubble velocity. In our simulations, the typical Keplerian velocity was ~ 400 km/s. Fig. 5 shows the position of the bubble front as a function of time. The solid line shows the expected position of the feature moving with the velocity of ~ 390 km/s. In the case of M87, the bubble's environment may not be very underdense compared to the ambient gas (since no clear X-ray holes have been seen) and the velocity of the bubble rise may be somewhat smaller. However, we believe that the above estimate of the rise velocity is approximately correct since the velocity depends only weakly (as the 0.5 power) on the bubble size and gas density gradients. This velocity defines a time scale of \sim few 10^7 years for the evolution of the bubble to the stage seen as a bright torus in Fig. 1.

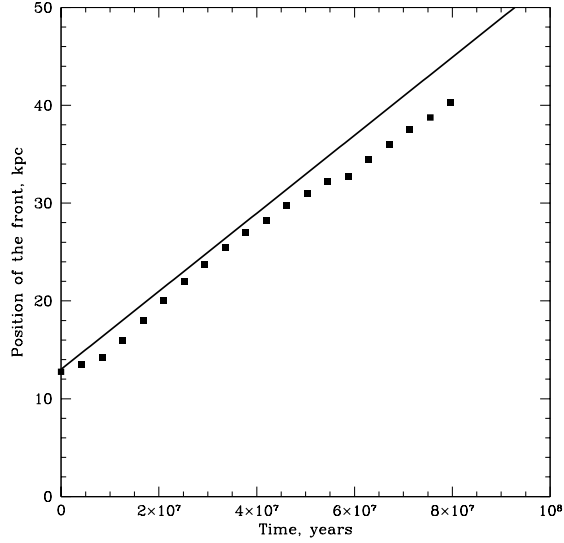


Fig. 5.— Position of the bubble front as a function of time. For comparison solid line shows the motion with the constant velocity of 390 km/s.

3.3. The rising bubble in synchrotron emission

In Figure 6 we show the results of the simulation at 327 MHz with two different values of the initial magnetic field strength. Note that the symmetry axis is perpendicular to the line of sight in the upper row (case 1) in this figure while it is at an angle of 45° with the line of sight (case 2) in the lower row. This leads to differences in the apparent distance of the upper edge of the bubble from the centre of the gravitational potential. From the radio observations of M87 we note that the well-defined eastern bubble is observed at a distance of roughly 25 kpc from the source centre. This corresponds to the third panel in the upper row of Figure 6, i.e. an age of the bubble of 42 Myrs, while for the simulation projected at an angle of 45° (lower row) the fourth panel at an age of 67 Myrs gives the correct projected distance.

Note here that these distances are for the primary bubble/vortex ring. Figure 6 clearly shows the presence of a secondary vortex ring which is closer to the centre. The appearance of this secondary ring is fairly dependent on the

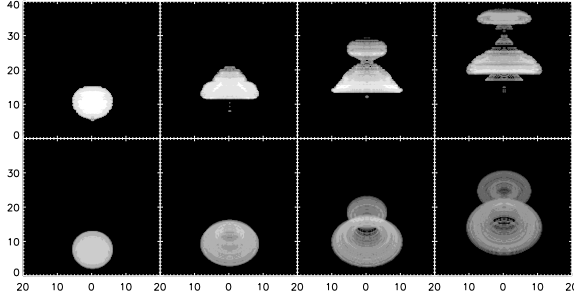


Fig. 6.— Synchrotron surface brightness at 327 MHz at four time steps. The upper row (case 1) shows the buoyant bubble for the case of the symmetry axis in the plane of the sky and $B \sim 6.5\mu\text{G}$ initially. The lower row (case 2) is for an inclination of 45° of the symmetry axis to the line of sight and $B \sim 2.9\mu\text{G}$ initially. From left to right both rows show the bubble at 4.2, 21, 42 and 67 Myrs after the start of the simulation. The filled contours bound regions of 0.017 (black), 0.04, 0.09, 0.2, 0.45, 1.0, 2.4, 5.5, 13, 28 and 66 (white) mJy per pixel, where a pixel is 250×250 pc at the distance of M87 (17 Mpc). The axes indicate the size of the bubble and its projected distance from the centre of the gravitational potential in kpc.

particular choice of initial conditions for our simulation (see Section 2 and Figures 3,4). However, in the case studied here, the synchrotron surface brightness of the secondary vortex ring exceeds that of the primary bubble. No such structure is observed in M87 and so we concentrate in the following discussion on the primary bubble.

In Section 1.1 we saw that the observed radio spectrum of the outer halo shows a break at about 3 GHz. To obtain a similar spectrum from the simulations we therefore expect from equation 1 with the ages given above that we need to set $B \sim 7\mu\text{G}$ for case 1 and $B \sim 4\mu\text{G}$ for case 2. For case 1 we therefore used $p = 2.3$ and an initial magnetic field strength of $6.5 \mu\text{G}$. For these values the spectral index of the primary bubble between 4.7 GHz and 10.6 GHz is -2.7 and that between 330 MHz and 1.5 GHz is -1.0 which compares well with the observed values of Rottmann et al. (1996, Section 1.1). For case 2 we set $p = 2.3$ $B = 2.9\mu\text{G}$. For this case the high frequency spectral index is found to be -3.0 while at the lower frequencies it

is -1.0 .

Solving equation 1 for t , we can determine the magnetic field B for which t reaches a maximum. This yields $B(t_{\max}) = B_{\text{CMB}}/\sqrt{3} \sim 2\mu\text{G}$. We have seen that the observed radio spectral indices require $\nu_{\text{break}} \sim 3$ GHz, corresponding to the t_{\max} of $\sim 10^8$ years. Thus, considering that the pressure and therefore the strength of the magnetic field decreases while the bubble rises, case 2 represents the maximum age the bubble may reach for any choice of B in order for our simulation to fit the observed spectrum. Since the projected distance of the bubble from the source centre is determined by the observations, this maximum age also defines the smallest angle of the symmetry axis of the bubble to the line of sight consistent with our simulation. For case 2, the smallest angle equals 45° .

The assumption of pressure equilibrium determines the initial energy density of the relativistic particles. We find $u_e \sim 4.2 \cdot 10^{-10}$ ergs cm^{-3} for both cases discussed. The energy density of the magnetic field is $1.7 \cdot 10^{-12}$ ergs cm^{-3} for case 1 and $3.4 \cdot 10^{-13}$ ergs cm^{-3} for case 2. This implies a severe departure from the equipartition condition of $u_B \sim u_e$ often assumed for synchrotron emitting plasmas. The peak surface brightness predicted in the region of the primary vortex ring is 55 mJy/pixel in case 1 and 2.4 mJy/pixel in case 2. The former agrees well with the observations (Owen et al. 2000, Section 1.1), however, even for this case the result implies that the volume filling factor of the relativistic plasma is very close to unity. This poses a serious problem for our assumption that the relativistic fluid does not influence the overall dynamics of the buoyant bubble. Furthermore, we neglected any possible contribution of the relativistic ions and thermal plasma to the pressure inside the bubble, which would further reduce its synchrotron emissivity.

The problems discussed above arise from the life time of the synchrotron emitting particles being short compared to the dynamical time scale of the structure. This generic problem of buoyant models was first noted by Gull & Northover (1973). In the following we discuss various solutions.

From Figure 6 we find that the diameter of our primary bubble is smaller than the largest diameter of the eastern bubble observed in M87. As

we show in Section 3.2, the rise time of the bubble is correlated with its size. It is therefore quite possible that the eastern bubble in M87 is somewhat younger than our simulations suggest. If true, then the younger age would imply a stronger magnetic field in the bubble, in order to explain the observed aged spectrum, which in turn would allow a smaller volume filling factor for the relativistic fluid.

The buoyant bubble may also be filled mainly by a weak magnetic field interspersed with regions of a much higher field strength but small volume filling factor. The relativistic electrons may then survive for a much longer time in the mainly weak magnetic field and only diffuse slowly into the regions of greater field strengths which are responsible for most of the observed synchrotron emission (Eilek, Melrose & Walker 1997). Subsonic turbulence can also enhance the energy density of the magnetic field in the regions with initially weak field (e.g. Eilek, Owen and Zhou 1999).

If the magnetic field in the buoyant bubbles is stronger than estimated above and rather homogeneous then *in situ* acceleration of relativistic particles is required. In this case, the age of the buoyant bubble cannot be constrained from radio observations. The two latter mechanisms were also discussed by Owen et al. (2000) to explain the radio emission of the outer halo of M87.

The fundamental conclusion of these simulations is that one can reproduce the observed radio brightness and the break in the spectrum of the torus-like feature in M87 assuming that (i) the bubble, filled with the relativistic plasma, is in pressure equilibrium with the thermal gas, (ii) the initial magnetic field strength is relatively low so as to prolong the lifetime of the electrons and (iii) no *in situ* reacceleration of particles or generation of magnetic field is occurring during the bubble evolution. However the equipartition condition is to be sacrificed and the parameter space allowed by these assumptions is rather tight. It is likely that the real situation is much more complex than was assumed in the simple model discussed above.

3.4. The rising bubble in X-ray emission

As is clear from Fig.3, the bubble captures ambient gas during its transformation to a torus and

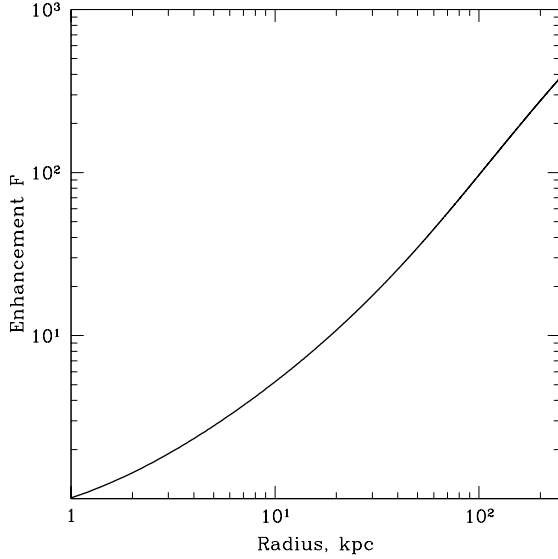


Fig. 7.— Volume emissivity of the uplifted and adiabatically expanded gas relative to the ambient gas. The curve is normalized to unity at 1 kpc. The enhancement factor, $F(r)$, is the ratio of the emissivity of the gas uplifted from 1 kpc to r to that of the ambient gas at r . The ratio $F(r_2)/F(r_1)$ characterizes the factor by which volume emissivity of the gas uplifted from r_1 to r_2 exceeds the volume emissivity of the ambient gas at r_2 .

then uplifts this gas to larger radii. Since all motions in our simulations are subsonic, this uplifted gas remains in approximate pressure equilibrium with the ambient gas at larger radii. The volume emissivity of this gas can be compared with the volume emissivity of the ambient gas:

$$\begin{aligned}\epsilon_u &= n_u^2 \Lambda(T_u) \\ \epsilon_a &= n_a^2 \Lambda(T_a),\end{aligned}\quad (5)$$

where n and T are the density and temperature of the uplifted and ambient gas respectively, $\Lambda(T)$ is the emissivity in a given energy band. If we assume adiabatic evolution of the entrained and uplifted gas then:

$$n_u = n_{a,0} \left(\frac{P_a}{P_{a,0}} \right)^{1/\gamma} = n_a \frac{T_a}{T_{a,0}} \left(\frac{P_a}{P_{a,0}} \right)^{1/\gamma-1} \quad (6)$$

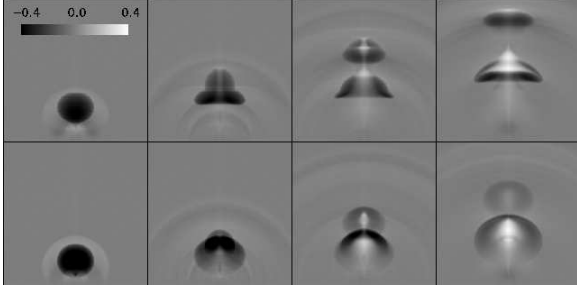


Fig. 8.— Expected X-ray morphology of the bubble for the same times as in Fig.6. Each box is 40 by 40 kpc. The figures shows the relative deviation of the X-ray surface brightness (in the ROSAT energy band) with respect to the unperturbed X-ray emission of the cooling flow. The darker regions are X-ray underluminous and lighter regions are X-ray bright. Black corresponds to regions dimmer by 40% (or more) than the unperturbed value and white corresponds to regions brighter by 40% (or more) than the unperturbed value.

$$T_u = T_{a,0} \left(\frac{P_a}{P_{a,0}} \right)^{1-1/\gamma}, \quad (7)$$

where the subscript 0 stands for the values of the uplifted gas at its initial location where it was captured by the rising bubble. Thus the uplifted gas will have an emissivity which is higher than the ambient gas by a factor:

$$F = \frac{\epsilon_u}{\epsilon_a} = \left(\frac{T_a}{T_{a,0}} \right)^2 \left(\frac{P_a}{P_{a,0}} \right)^{2/\gamma-2} \times \frac{\Lambda(T_u)}{\Lambda(T_a)}. \quad (8)$$

The first term (without ratio of the cooling functions) is shown in Fig.7. One can see that in the cooling flow conditions (density decreases with distance while temperature increases) the emissivity of the uplifted gas greatly exceeds the emissivity of the ambient gas if the displacement is large. The ratio $\Lambda(T_u)/\Lambda(T_a)$ (when the temperatures are of the order of keV and soft X-ray band is considered) further increases the brightness of the uplifted gas with respect to the ambient gas.

In order to illustrate how the X-ray surface brightness will be modified by the presence of the rising bubble of radio emitting plasma and lumps of the uplifted cold gas we calculated the projected surface brightness distribution (for the ROSAT energy band from 0.5 to 2 keV) for several stages

of the bubble evolution. When calculating these maps we assumed axial symmetry and assumed that the axis of the bubble is either perpendicular to the line of sight (upper row of images in Fig.8) or that the angle between the line of sight and bubble axis is 45° (lower row of images in Fig.8). Fig.8 shows the relative deviation of the X-ray surface brightness from the unperturbed value of the surface brightness at the same distance from the center. As expected the “trunk” of the mushroom is brighter than the surrounding regions.

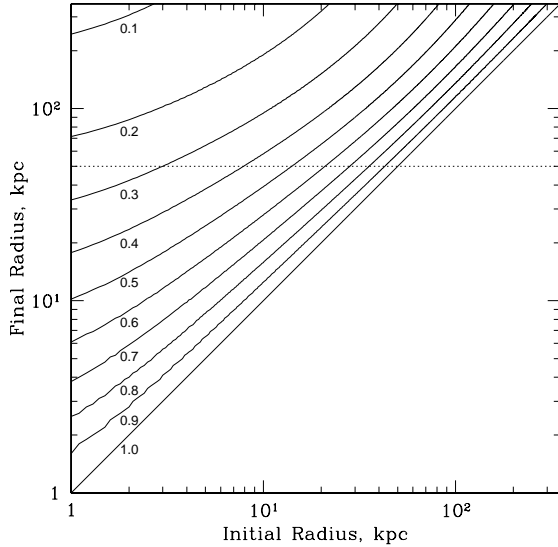


Fig. 9.— The maximum radius to which the bubble can rise depending on its initial location and the volume fraction of gas, captured during the transformation of the bubble into a torus. It is assumed that the bubble consists of separate lumps of radio and X-ray emitting plasmas bound together. Each curve corresponds to a given volume fraction (labels under the curves) of entrained gas added to the bubble near the original bubble position. If, for example, the large circular radio emission regions are located at a distance of 50 kpc from the center (horizontal dotted line) then a bubble could rise from 5 kpc to 50 kpc with the amount of “entrained” gas corresponding to approximately 35% of its initial volume.

Abundance gradients are frequently observed in cluster cooling flows (e.g. Matsumoto et al. 1996).

If our interpretation of the X-ray features as uplifted lumps of gas is correct, then one would expect the abundance in these regions to be higher than in the surrounding regions. This can be tested with Chandra and XMM.

3.5. The pancake stage

If the lumps of radio and X-ray emitting plasmas in the bubble are bound together (e.g. by magnetic stresses as in the multiphase cooling flow picture of Nulsen (1986)) then one can calculate the maximum radius to which the whole bubble can rise for given volume fractions of “entrained” gas and (weightless) radio emitting plasma (see eq. (6) in Churazov et al. 2000). Shown in Fig.9 is the dependence of the final position of the bubble on the initial position and fraction of the bubble volume occupied by the entrained gas, captured near the initial location of the bubble. At this final location, the average mass density of the bubble (consisting of separate lumps of radio and X-ray emitting plasma) is equal to the density of the ambient gas. At the final position the bubble will spread along the equipotential (isodensity) surface and may form a pancake-like structure. Such a late stage in bubble evolution was not simulated here, but it is observed for powerful atmospheric explosions. The X-ray appearance of the bubble at this stage crucially depends on whether mixing of radio and X-ray emitting plasmas is microscopic or macroscopic (Böhringer et al. 1995, Nulsen 1997)

If on the contrary lumps of radio emitting plasma are not bound to the captured lumps of the thermal gas, then radio bubbles will continue to rise along the pressure gradient and will eventually leave the central cooling flow region. Overdense lumps of captured gas will separate from the bubbles and fall back towards the central region. One possible example of overdense material having fallen back toward the central galaxy may be found in A1795. Cowie et al. (1983) reported a remarkable $\sim 45''$ (41 kpc long for the Hubble constant of 100 km/s/Mpc) filamentary emission line ($\text{H}\alpha + [\text{NII}]$) chain originating near the central cD galaxy.

3.6. The circular radio emission regions

The largest structures visible in Figure 1 are the two almost circular low surface brightness emission regions to the northeast and southwest of the centre. Owen et al (2000) suggest that these are spherical bubbles of radio plasma seen in projection. In this case, they may receive substantial amounts of energy from the inner lobes which contain the active jet. Alternatively one can identify the circular emission regions seen in the radio images with earlier bubbles that have reached their isodensity distance and are now in the process of spreading and forming pancake-like structures (see previous Section). We stress again that this requires that either relativistic and thermal particles are mixed on the microscopic scales or the lumps of relativistic plasma and the ambient medium are bound together.

Furthermore, this interpretation implies that the circular emission regions are not the projections of nearly spherical lobes but rather that they are thin pancake-like structures (see Fig. 1). If these pancakes lie close to the line of sight in front of and behind the inner radio lobes, this naturally explains their almost circular appearance. The thickness of the pancakes may then be estimated from their radio properties as follows:

The total pressure exerted by a radio plasma is given by

$$p_{\text{rel}} = \frac{1}{3} (u_e + u_B) = \frac{1}{3} \left(G(p) \frac{L_\nu}{V} B^{-3/2} + \frac{B^2}{8\pi} \right), \quad (9)$$

where L_ν is the synchrotron luminosity of the plasma at frequency ν and V is the volume it occupies. $G(p)$ only depends on the slope of the energy distribution of the relativistic particles and is given by Longair (1991). As the spreading bubble is in pressure equilibrium with the surrounding atmosphere at p_{atm} , we have $p_{\text{atm}} = p_{\text{rel}} + p_{\text{th}}$. p_{th} is the contribution of any thermal material mixed in with the radio plasma. At a given point in the outer halo we can convert the measured surface brightness into a luminosity, L_ν , which is emitted by the material within $V = Al$, with A being the surface area at the source covered by the beam of the observing telescope and l the length of the line of sight through the pancake. Substituting from equation 9 this yields

$$l = G(p) \frac{L_\nu}{A} B^{-3/2} \left[3p_{\text{atm}} x - \frac{B^2}{8\pi} \right]^{-1}, \quad (10)$$

where we parameterize $p_{\text{th}} = (1 - x)p_{\text{atm}}$. Obviously $l \rightarrow \infty$ when the term in square brackets in equation 10 tends to zero. In this case the bubble is pressure supported by the thermal material and the magnetic field and the energy density and therefore also the density of the relativistic particles becomes very small.

The fact that emission at 10.6 GHz is still observed from the pancakes suggests that, unless significant re-acceleration has taken place, they are efficiently conserving their relativistic particles. Following the discussion in Section 2.2, it is therefore likely that the magnetic field in the pancakes is close to $B_{\text{CMB}}/\sqrt{3}$. This allows for the maximum age of the radio plasma given the observed spectrum. Independent evidence for the strength of the magnetic field comes from observations of the EUV excess emission from the region of the radio halo of M87. Berghöfer et al. (1999) show that if this excess is due to inverse Compton scattering of the CMB by the relativistic electrons in the halo, then $B \sim 3\mu\text{G}$. Note however, that the radio emission at high frequencies may also be explained if other processes like particle diffusion between regions of different strength of the magnetic field or *in situ* re-acceleration are at work (Section 2.2 and Owen et al. 2000).

In Figure 10 we plot equation 10 for $B = B_{\text{CMB}}/\sqrt{3}$ and p_{atm} as given by our unperturbed model atmosphere (see Section 2) at 50 kpc from the centre of the gravitational potential. To indicate the variation of this thickness with the height to which the bubbles rises, we also plot l for a distance of 10 kpc. Here we have used a surface brightness of the halo of 25 mJy beam^{-1} at 327 MHz (Owen et al. 2000). Clearly, the circular emission regions must be thin layers as long as they are not almost exclusively supported by the pressure of any thermal material inside them. In Section 2.2 we demonstrated that this is unlikely at least for the vortex rings observed in M87 which are the progenitors of the pancakes according to our interpretation. Considerable quantities of thermal gas may be mixed with the material of the bubble after the buoyant phase. However, in this case the bubble and the mixed-in material are

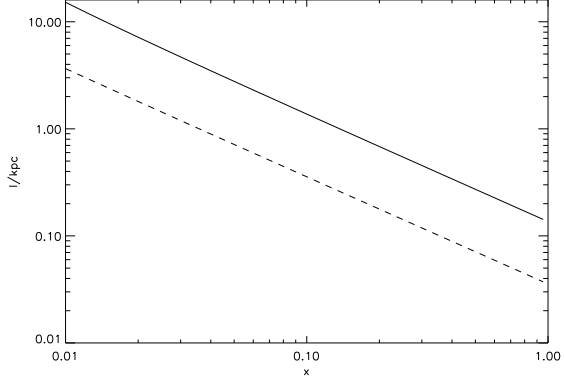


Fig. 10.— Thickness of the circular emission regions in the radio halo of M87 as a function of the thermal pressure support (see text). The distance of the emission region from the centre of the gravitational potential is either 50 kpc (solid line) or 10 kpc (dashed line).

in pressure equilibrium and so x cannot be much smaller than 1.

In projection, both pancakes cover the inner lobes of M87 (Figure 1). According to our interpretation one of them must lie between us and the inner lobes. From the RM differences reported by Owen et al. (1990) this should be the pancake to the southwest. We therefore expect some contribution of the pancakes to the observed Faraday rotation towards the inner radio lobes. Assuming that $l \sim 3 \text{ kpc}$ we find $\text{RM} = 74 \text{ rad m}^{-2}$ and $\text{RM} = 13 \text{ rad m}^{-2}$ for the height of the pancake in the atmosphere of 10 kpc and 50 kpc, respectively. Compared to the observed values, 750 rad m^{-2} in the western lobe and 2000 rad m^{-2} in the eastern lobe, this is small. However, note that the inner lobes are presumably also covered by the ‘trunks’ connecting the vortex rings with the source centre (Figure 1). It is likely that we observe these structures in projection and so they may cover considerable lengths along the line of sight towards the inner lobes giving rise to large RM.

Owen et al (2000) have noted the sharp boundary of the M87 halo which is traced by all observations at different frequencies and they argue that this excludes a dominant diffusive transport process for the relativistic plasma. In the proposed model the radius and sharpness of the boundary

is naturally explained by the height to which buoyant bubbles can rise. Also the complicated structure of the outer halo may in this model reflect several layers of partly fragmented bubbles.

3.7. Total energy budget

The X-ray luminosity of the whole cooling flow region around M87 is about 10^{43} erg/s. On the other hand, estimates of the total energy supplied by the jet to the ICM give a much larger value of $\sim 10^{44}$ erg/s (e.g. Owen, Eilek and Kassim 2000). If all this energy can be dissipated into the thermal gas in the cooling flow region then the cooling flow should instead be a “heating” outflow (Owen, Eilek and Kassim 2000), at least at the present moment. The situation may be transient (and it is likely that it is) so that inflow and outflow periods are alternating depending on the status of the AGN activity (Tucker and David 1997, Binney 1999, Owen, Eilek and Kassim 2000). We speculate below on the consequences of a large input of power in the form of relativistic plasma into the cooling flow region.

First, if we assume that bubbles are rising approximately with the Keplerian velocity of ~ 400 km/s and this velocity limits the growth of the original bubble due to the jet input power $L: \frac{\gamma}{\gamma-1} P_0 4\pi r^2 v = L$, where P_0 is the ambient gas pressure, $\gamma = 4/3$ is the adiabatic index of the relativistic gas in the bubble, r is the size of the bubble. Substituting $L \sim 10^{44}$ erg/s, $P_0 \sim 2 \times 10^{-10}$ erg cm^{-3} and $v \sim 400$ km/s we get $r \sim 5$ kpc, which is approximately the size of the inner lobes surrounding the jets.

The inner lobes break loose (during $t \sim r/v \sim 10^7$ years) and form bubbles which then subsonically rise through the cluster atmosphere (Gull and Northover 1973). At any given moment, thermal gas tries to settle in the potential of the cluster in order to form a nondecreasing entropy profile. Rising bubbles cause convective motions in the gas and cause mixing of lumps of thermal gas with different entropies. Using tracer particles added to the thermal gas we estimated total amount of cool gas transported by the bubble after $\sim 8 \times 10^7$ years: some $3-4 \times 10^7 M_\odot$ of the thermal gas has been uplifted from below 15 kpc to above 35 kpc. Much larger masses of gas has undergone smaller displacement by that time: $\sim 1.3 \times 10^8 M_\odot$ has

been moved from below 14 kpc to above 25 kpc. Although these are very crude estimates, which are sensitive to the particular initial and boundary conditions adopted in our simulations, one can expect that if the bubbles are launched approximately every 10^7 years then they are able to transport some $1-10 M_\odot$ of the cold gas per year from the center to the periphery of the cooling flow. Interestingly this value is comparable with the mass deposition rate in M87 estimated from the X-ray data. One can further list several important consequences of the convection induced by the rising bubbles:

- Due to uplifted cold gas, the X-ray surface brightness distribution should be shallower than in the absence of bubbles. The entropy profiles also flatten.
- If the bubbles are formed and are rising systematically over some preferred direction then the cold gas will be continuously uplifted over this direction while it will be flowing inward in other directions.
- Thermal instabilities can effectively take place within an environment of extensive convective motions. As a result, distributed mass deposition can naturally occur.
- Overdense lumps of thermal gas, uplifted by the rising bubbles, may fall back (when separated from the “carrier” buoyant bubble) to the central region thereby producing filamentary structures, stretching radially from the galaxy.

Even if the bubbles are not mixed on microscopic scales with the thermal plasma and are able to eventually leave the cooling flow region, most of the energy has to be deposited in the thermal gas (if there is a strong contrast in pressure between the inner and outer regions of the cooling flow). This does not mean that the thermal gas is heated directly by the relativistic plasma. The energy instead goes mostly into subsonic motions of the gas. It is difficult to accurately estimate what fraction of energy of these subsonic motions will eventually be dissipated locally and what fraction will be carried (e.g. by sound waves) away from the cooling flow region. If the jet power is

indeed $\sim 10^{44}$ erg/s then even a modest 10% efficiency of local dissipation into heat should be enough to exceed the radiative cooling of the gas. The gas then heats up, but this heating is distributed through the large volume involved in the convective motion. If strong input from AGN is maintained for a very long period then a core with a flat entropy profile will be formed and the size of this core will grow with time. Eventually such a process is capable of completely eliminating the cooling flow, unless the power of an AGN is in turn regulated by the conditions in the cooling flow region as discussed by Tucker and David (1997), Binney (1999), Owen, Eilek and Kassim (2000). In M87, heating at a rate of $\sim 5 \times 10^{43}$ ergs/s would eliminate the cooling flow for $\sim 10^8$ years. This is comparable to the age of the largest radio structures. On the other hand, the complicated radio halo morphology perhaps suggests that periods of high AGN activity have alternated with the periods of low AGN power. We note here that dissipation of the subsonic motions into heat may take a much longer time than the characteristic time of the bubble rise and therefore the actual gas heating rate may be related to the AGN activity averaged over a long period of time.

4. Conclusions

Buoyant bubbles of cosmic rays slowly rising through the cooling gas can qualitatively explain the complicated radio and X-ray morphology of the central 40 kpc region around M87. Torus-like features seen in the radio may be similar to the "mushrooms" which appear in Rayleigh-Taylor unstable configurations: as the fluid rises through the ambient medium, Kelvin-Helmholtz instabilities create the torus-like head of the "mushroom". The excess X-ray emission trailing some prominent features in radio could be due to the cold gas captured by the rising bubbles and uplifted to large distances from the central source.

Our model is of course highly oversimplified and is not intended to closely reproduce the M87 environment. Clearly more detailed simulations are needed, perhaps in 3D, which would also follow the formation of the initial bubble (and possibly continuous energy input) and include radiative cooling.

Rising bubbles give rise to a strong convection

in the cooling flow region. Convection flattens X-ray surface brightness and entropy profiles in the cooling flow. Convection may promote distributed mass deposition in the cooling flow and formation of the filaments. If more than 10% of the energy supplied by the jet is dissipated into heat in the cooling flow region then eventually large cores with a flat entropy profile may be formed.

We are grateful to Alexei Krutsuk, Nail Ingogamov, Christine Jones, Nail Sibgatullin and Henk Spruit for useful discussions. This research has made use of data obtained through the High Energy Astrophysics Science Archive Research Center Online Service, provided by the NASA/Goddard Space Flight Center.

REFERENCES

Berghöfer T.W., Bowyer S., Korpela E., 1999, in H. Böhringer, L. Feretti, and P. Schuecker (eds.), *Diffuse thermal and relativistic plasma in galaxy clusters*. MPE, p. 207

Binney, J. 1999, Berlin Springer Verlag Lecture Notes in Physics, 530, 116

Biretta, J. A. 1999, Berlin Springer Verlag Lecture Notes in Physics, 530, 159

Böhringer, H., Voges, W., Fabian, A. C., Edge, A. C. and Neumann, D. M. 1993, MNRAS, 264, L25

Böhringer, H., Nulsen, P. E. J., Braun, R. and Fabian, A. C. 1995, MNRAS, 274, L67

Böhringer, H., 1999, *Diffuse Thermal and Relativistic Plasma in Galaxy Clusters*, eds. H.Böhringer, L.Feretti, P.Schuecker, MPE Report 271, 115

Bolton J.G., Stanley G.J., Slee O.B., 1949, Nature, 164, 101

Churazov, E., Forman, W., Jones, C. and Böhringer, H. 2000, A&A, 356, 788

Cowie, L. L., Hu, E. M., Jenkins, E. B. and York, D. G. 1983, ApJ, 272, 29

Eilek, J. A., Melrose, D. B. and Walker, M. A. 1997, ApJ, 483, 282

Eilek, J., Owen, F. and Zhou, F. 1999, Berlin Springer Verlag Lecture Notes in Physics, 530, 136

Fabian A.C., Sanders J.S., Ettori S., Taylor G.B., Allen S.W., Crawford C.S., Iwasawa K., Johnstone R.M., Ogle P.M., 2000, MNRAS, accepted, astro-ph/0007456

Feigelson, E. D., Wood, P. A. D., Schreier, E. J., Harris, D. E. and Reid, M. J. 1987, ApJ, 312, 101

Gull, S.F., Northover, K. J. E. 1973 Nature, 244, 80

Harris D.E., Owen F.N., Biretta J.A., Junor W., 1999, Diffuse Thermal and Relativistic Plasma in Galaxy Clusters, eds. H. Böhringer, L. Feretti, P. Schuecker, MPE Report 271, 111

Huang, Z. and Sarazin, C. L. 1998, ApJ, 496, 728

Kaiser C.R., Dennett-Thorpe J., Alexander P., 1997, MNRAS 292, 723

Kassim, N. E., Perley, R. A., Erickson, W. C. and Dwarakanath, K. S. 1993, AJ, 106, 2218

Landau, L.D., Lifshitz, E.M., 1963, Fluid mechanics, Pergamon Press

Leahy J.P., 1991, in P. A. Hughes (ed.), Beams and jets in astrophysics. Cambridge University Press, p. 100

Longair M.S., 1991, *High energy astrophysics*, Cambridge University Press

Matsumoto, H., Koyama, K., Awaki, H., Tomida, H., Tsuru, T., Mushotzky, R. and Hatsukade, I. 1996, PASJ, 48, 201

McNamara, B. R., O'Connell, R. W. and Sarazin, C. L. 1996, AJ, 112, 91

McNamara, B. R., Wise, M., Nulsen, P. E. J., David, L. P., Sarazin, C. L., Bautz, M., Markevitch, M., Vikhlinin, A., Forman, W. R., Jones, C. and Harris, D. E. 2000, ApJ, 534, L135

Mills B.Y., 1952, Nature, 170, 1063

Norman, M.L., Smarr, L., Winkler, K.-H., Smith, M.D., 1982, A&A, 113, 285

Nulsen, P. E. J. and Böhringer, H. 1995, MNRAS, 274, 1093

Nulsen, P. E. J. 1986, MNRAS, 221, 377

Nulsen, P. E. J. 1997, ASP Conf. Ser. 115: Galactic Cluster Cooling Flows, 135

Onufriev, A.T. 1967, Zhurnal Prikladnoi Mekhaniki i Tekhnicheskoi Fisiki, 2, 101

Owen F.N., Eilek J.A., Kassim N.E., 1999, Diffuse Thermal and Relativistic Plasma in Galaxy Clusters, eds. H. Böhringer, L. Feretti, P. Schuecker, MPE Report 271, 107

Owen F.N., Eilek J.A., Kassim N.E., 2000, ApJ: submitted, astro-ph/0006150

Owen F.N., Eilek J.A., Keel W.C., 1990, ApJ 362, 449

Peres, C. B., Fabian, A. C., Edge, A. C., Allen, S. W., Johnstone, R. M. and White, D. A. 1998, MNRAS, 298, 416

Rottmann H., Mack K.-H., Klein U., Wielebinski R., 1996, A&A 309, L19

Stone, J.M., Norman, M.L., 1992a, ApJS, 80, 753

Stone, J.M., Norman, M.L., 1992b, ApJS, 80, 791

Tucker, W. and David, L. P. 1997, ApJ, 484, 602

Walters, J.K. Davidson, J.F. 1963, J.Fluid.Mech., 17, 321

Zhidov, I.G. Meshkov, E.E. Popov, V.V. Rogachev, V.G. Tolshmyakov A.I. 1977, Zhurnal Prikladnoi Mekhaniki i Tekhnicheskoi Fisiki, 3, 75